

## Frequency- and magnetic-field-dependent properties of ordered magnetic nanoparticle arrangements

Nils Neugebauer,<sup>1,\*</sup> Toni Hache<sup>2,3</sup>, Matthias T. Elm,<sup>1,4,5</sup> Detlev M. Hofmann,<sup>1,4</sup> Christian Heiliger,<sup>4,6</sup> Helmut Schultheiss<sup>6,7</sup> and Peter J. Klar<sup>1,4</sup>

<sup>1</sup>*Institute of Experimental Physics I, Justus Liebig University Giessen, Heinrich-Buff-Ring 16, 35392 Giessen, Germany*

<sup>2</sup>*Helmholtz-Center Dresden-Rossendorf, Institute of Ion Beam Physics and Materials Research, Bautzner Landstraße 400, 01328 Dresden, Germany*


<sup>3</sup>*Institute for Physics, Technische Universität Chemnitz, 09107 Chemnitz, Germany*

<sup>4</sup>*Center for Materials Research (ZfM/LaMa), Justus Liebig University Giessen, Heinrich-Buff-Ring 16, 35392 Giessen, Germany*

<sup>5</sup>*Institute of Physical Chemistry, Justus Liebig University Giessen, Heinrich-Buff-Ring 17, 35392 Giessen, Germany*

<sup>6</sup>*Institute for Theoretical Physics, Justus Liebig University Giessen, Heinrich-Buff-Ring 16, 35392 Giessen, Germany*

<sup>7</sup>*Technische Universität Dresden, 01062 Dresden, Germany*

 (Received 5 November 2020; revised 16 February 2021; accepted 15 March 2021; published 24 March 2021)

We present investigations of the frequency and magnetic field dependent properties of ordered magnetic nanoparticles (MNPs) arrangements consisting of magnetite ( $\text{Fe}_3\text{O}_4$ ) nanoparticles with an average diameter of 20 nm by employing micro Brillouin light scattering microscopy. We utilized electron beam lithography to prepare hexagonally arranged, circularly shaped MNP assemblies consisting of a single layer of MNPs using a variant of the Langmuir-Blodgett technique. By comparing the results with nonstructured, layered superlattices of MNPs, further insight into the influence of size and geometry of the arrangement on the collective magnetic properties is obtained. We show that at low static external field strengths, two signals occur in frequency dependent measurements for both nonstructured and structured assemblies. Increasing the static external field strength results in a sharpening of the main signal, while the satellite signal decreases in its intensity and increases in its linewidth. The occurrence of multiple signals at low external field strengths is also confirmed by sweeping the static external field and keeping the excitation frequency constant. Furthermore, two-dimensional spatial mapping of the resonances reveals that the main and the satellite signal originate from the center and the edge, respectively, of a single circular MNP assembly. Micromagnetic simulations confirm these assignments and the dependence of the two signals on the static external field strength, justifying an interpretation of the observed characteristics in terms of different local environments of MNPs forming the MNP assembly.

DOI: [10.1103/PhysRevB.103.094438](https://doi.org/10.1103/PhysRevB.103.094438)

### I. INTRODUCTION

The development and improvement of novel electronic devices employed in technological applications has driven modern science to find and unveil new approaches, e.g., in preparing novel functional units in electronic circuits or magnetic devices. In recent years, conventional fabrication processes, in which top-down and bottom-up techniques were used to create structured thin films, have been challenged by various novel experimental approaches, which utilize nanoscale components such as magnetic quantum dots, nanoclusters, or likewise nanoparticles [1–8]. Using nanoparticles as building blocks of devices yields additional degrees of freedom to manipulate the fundamental device characteristics, which is not possible using bulk materials only [9–13]. Employing nanoparticles has therefore attracted great and increasing interest during the past decades, since the controllability of their shape, size, composition [14], and arrangement in highly ordered structures is steadily advancing [5,11,14–

17]. However, the potential use of nanoparticles in devices for a specific application requires a detailed knowledge of the fundamental interactions of the nanoparticles with their environment. In particular in the case of magnetic nanoparticles this also includes interactions between the nanosized constituents themselves and, thus, their collective behavior [12,18–21]. The fundamental interactions between magnetic nanoparticles are governed by dipole interactions, since the magnetic core of each particle is surrounded by an organic shell (oleic acid), which prevents an electronic contact between the particles and, thus, e.g., exchange interaction between them [22–24]. Certainly, dipole interactions between magnetic nanoparticles become more and more important as the size of the MNPs themselves and the lateral extension of their arrangement in ordered and densely packed structured superlattices decreases [25–29]. In the light of a continuous miniaturization of electronic circuits and magnetic devices, the finite size and the shape of the functional unit becomes more and more important as the surface to volume ratio increases with decreasing arrangement size [30,31]. Depending on the unit's size and shape different local environments occur, which makes a detailed understanding of the interaction

\*Nils.Neugebauer@physik.uni-giessen.de

of the magnetic moment of a MNP with its environment indispensable.

Here we present an investigation of the dipolar interaction between MNPs within circularly structured as well as nonstructured, layered superlattices. Micro Brillouin light scattering ( $\mu$ BLS) microscopy is employed to investigate frequency and external field dependent properties of the corresponding nanoarrangements. On these length scales, dipole interactions between the different constituents determine the overall magnetic properties. Obtaining a deep understanding of the collective dipolar behavior of the MNP arrangements and of their response to the simultaneously applied external magnetic field and microwave field represents the motivation of this work. Insight into the collective properties of the MNP arrangements is further provided by carried out micromagnetic simulations of the corresponding model systems, which enables one to determine the internal dipole field distribution and to identify the active regions of the arrangement yielding a specific resonant excitation.

## II. METHODS

### A. Sample preparation

The preparation of the ordered MNP arrangement for the  $\mu$ BLS experiments comprises two main fabrication steps. First, a microwave antenna is defined on a high-resistance silicon wafer ( $>10\,000\ \Omega/\text{cm}$ ). The antenna is later used to excite magnetic oscillations within the corresponding magnetic structure in the  $\mu$ BLS experiment. For this purpose, the wafer is coated with a 300-nm-thick PMMA A4 950 K layer. It allows one to pattern the antenna by electron beam lithography (EBL) using a low dose of  $D = 1000\ \mu\text{C}/\text{cm}^2$  (at an acceleration voltage of 15 kV) during an electron beam lithography (EBL) process. When a low dose is used, PMMA serves as a positive resist. Thus the exposed areas are dissolved during the development process, i.e., during the immersion in an isopropanol-water solution (volume ratio 2:1) for 45 seconds. Subsequently, a 5-nm-thick chromium layer serving as an adhesion aid and a 100 nm gold layer as the antenna material are deposited using electron beam evaporation. The residual PMMA with the metal layers on top are removed by placing the wafer in an ultra sonic bath filled with acetone for 10 minutes at  $20^\circ\text{C}$  yielding the gold antenna of the desired shape.

Afterwards, the second fabrication step is performed. It comprises the formation of the MNP arrangement on top of the antenna structure defined on the silicon wafer. Following the technique proposed by Pang [32] *et al.*, magnetite ( $\text{Fe}_3\text{O}_4$ ) MNPs with an average diameter of  $d_{\text{NP}} = 20\ \text{nm}$  suspended in toluene (standard variation  $\sigma = 5\ \text{nm}$ , particle concentration  $c \sim 4.5 \times 10^{13}$  particles/mL - Sigma-Aldrich product number: 725366) are diluted by adding 50 parts of toluene as solvent to one part of the original suspension. In order to enable patterning of the MNPs during the EBL exposure, five parts of 950 K PMMA A4 are added to the diluted MNP suspension. To ensure good homogeneity of the suspension, the mixture is placed in an ultrasonic bath for 10 minutes at room temperature. Subsequently 100  $\mu\text{L}$  of the MNP-PMMA-toluene mixture are pipetted onto a water

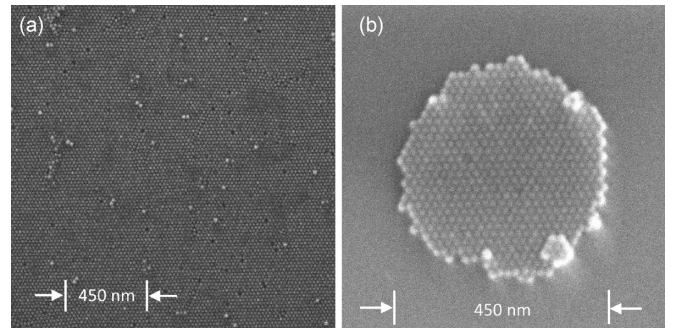


FIG. 1. (a) Using a variant of the Langmuir-Blodgett technique, a mixture of MNPs suspended in toluene and PMMA is pipetted onto a water subphase. During the evaporation of the solvent, a self-assembling process takes place leading to a hexagonal arrangement of a single layer of MNPs which can be transferred to a silicon wafer substrate. (b) After the EBL exposure with high doses and a subsequent development process, patterned MNP arrangements are synthesized.

subphase within a beaker of 10 cm in diameter. After 30 minutes, the solvent is entirely evaporated and a monolayer of MNPs separated by PMMA is formed. The MNP monolayer is then transferred onto a previously structured silicon wafer resulting in hexagonally arranged MNPs as shown in Fig. 1(a). PMMA between the individual particles can act as a negative resist when using high doses during the EBL exposure. Thus, by using a high dose of  $D = 15\,000\ \mu\text{C}/\text{cm}^2$  in a subsequent EBL process, exposed areas of the MNP monolayer remain after resist development yielding structured MNP arrangements. Figure 1(b) shows an example of a circular MNP arrangement with a diameter of  $\sim 450\ \text{nm}$  prepared in this way. The preparation of nonstructured, layered superlattices is achieved by increasing the concentration of MNPs in the MNP-PMMA-toluene mixture by a factor of 2, which leads to arrangements consisting of multiple layers up to eight layers thick.

### B. Brillouin light scattering microscopy

To investigate the dynamic properties of magnetic nanostructures, several techniques have been established to excite and detect magnetic oscillations of the corresponding magnetic system. Among these,  $\mu$ BLS has demonstrated an excellent capability of investigating frequency and external magnetic field dependent properties [21,33–35]. In the experiment, a sample is placed on a microwave antenna structure in an external magnetic field  $B_{\text{ext}}$ , and the response of the magnetic system is analyzed by exposing the sample to photons of a wavelength (frequency) of 532 nm (56 352 THz). In order to resonantly stimulate magnetic oscillations within the sample, the same spot on the sample is also excited with an external microwave field of a defined excitation frequency  $f_{\text{ext}}$ . The impinging laser photons can then interact with the magnetic excitations, which causes a frequency shift  $\Delta f_{\text{phot}}$  by inelastic scattering (Brillouin process). This frequency shift  $\Delta f_{\text{phot}}$  represents a distinct signature of the corresponding magnetic oscillation. Thus, measuring the intensity of the inelastically scattered photons for pairs of excitation frequency  $f_{\text{ext}}$  and

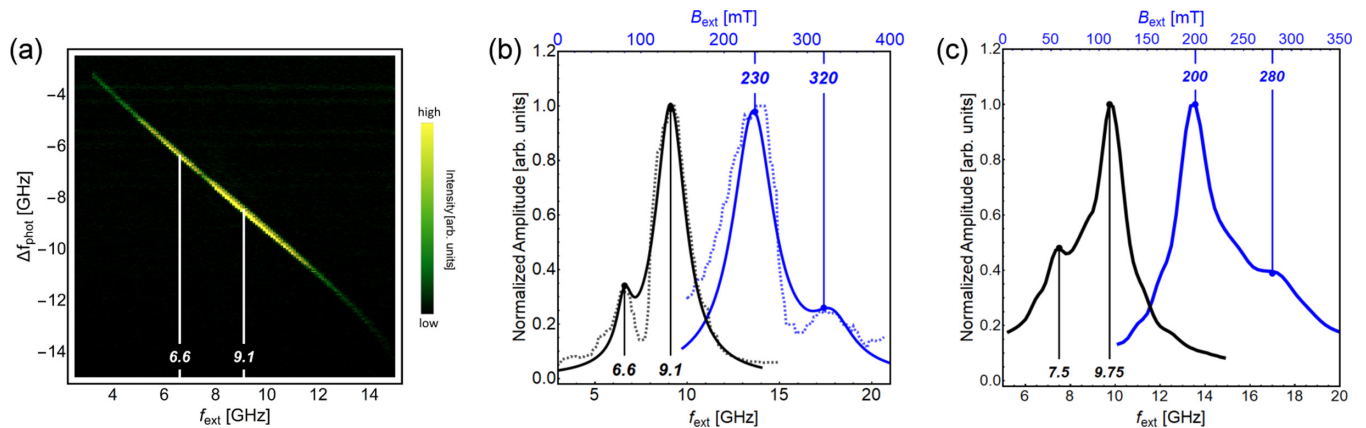


FIG. 2. (a)  $\mu$ BLS intensity of the circularly structured MNP arrangement shown in Fig. 1(b) detected in a microwave excitation frequency range between  $f_{\text{ext}} = 0$  GHz and 15 GHz as a function of the external excitation frequency  $f_{\text{ext}}$ . The data were recorded at an external field strength of  $B_{\text{ext}} = 230$  mT. Integrating the data for each  $f_{\text{ext}}$  leads to an accumulated spectrum as shown in (b) (black dashed curve). It is clearly visible that one main signal is present at  $f_{\text{ext}} = 9.1$  GHz, accompanied by a satellite signal located at  $f_{\text{ext}} = 6.6$  GHz. Keeping the excitation frequency constant at  $f_{\text{ext}} = 9$  GHz and sweeping the external field strength yields the corresponding accumulated field-dependent spectrum which also exhibits two signals (blue dashed curve). The continuous curves represent fits with two Lorentzian curves to the corresponding data. (c) Simulated  $f_{\text{ext}}$ - (black curve) and  $B_{\text{ext}}$ -dependent spectra (blue curve) of a hexagonally arranged, circularly shaped MNP assembly. The assembly has a diameter of 300 nm. The frequency-dependent spectrum was calculated for  $B_{\text{ext}} = 200$  mT, while the external field strength dependent spectrum was simulated for  $f_{\text{ext}} = 9.75$  GHz. Both spectra show a main peak accompanied by a satellite peak of lower intensity in agreement with the experimental results.

frequency shift  $\Delta f_{\text{phot}}$  yields insight into the magnetic characteristics of the system at constant  $B_{\text{ext}}$ . Furthermore, instead of analyzing the  $f_{\text{ext}}$ -dependent response of the magnetic structure at a constant magnetic field strength  $B_{\text{ext}}$ ,  $B_{\text{ext}}$ -dependent properties can also be examined for constant  $f_{\text{ext}}$  by measuring the intensity of inelastically scattered photons versus  $\Delta f_{\text{phot}}$  at different external field strength  $B_{\text{ext}}$ . The frequency and static magnetic field dependent  $\mu$ BLS experiments were performed at room temperature. All measurements were recorded in an excitation frequency range from  $f_{\text{ext}} = 0$  GHz to 15 GHz and a magnetic field range from  $B_{\text{ext}} = 100$  mT to 400 mT.

### C. Theoretical modeling

Micromagnetic modeling of the corresponding MNP arrangements is indispensable for evaluating the results obtained from the  $\mu$ BLS experiments, since the origin of the occurring signals is usually not entirely intuitive. To obtain deeper insight into the dynamic properties of such arrangements, a code has been developed for elucidating the associated characteristics. For details of this code, we refer the reader to our previous publications [36,37].

Since magnetite nanoparticles of diameters of less than 50 nm can be considered as single domain particles [38,39], each MNP can be represented by a single vector  $\vec{m}_i(\vec{r}, t)$  (where  $\vec{r}$  denotes the position vector and  $t$  the time) in the model. It is well known that the magnetization of magnetic nanoparticles is somewhat smaller than that of the bulk material. In our simulations, we assigned a magnetic moment of  $m = 2.2 \times 10^5 \mu_B$ , where  $\mu_B$  is the Bohr magneton, to each MNP, which is in good agreement with previous size dependent investigations of the magnetization [31,40–42]. A magnetic moment  $\vec{m}_i(\vec{r}, t)$  interacts only via dipole-dipole interaction with its neighboring moments. Solutions of the time evolution of the whole magnetic system  $\vec{M}(\vec{r}, t) = \sum_i \vec{m}_i(\vec{r}, t)$

under an external exciting microwave field  $\vec{B}_{\text{mw}}(t, f_{\text{ext}})$  are then obtained by numerical integration of the equation of motion described by the Landau-Lifshitz-Gilbert equation [43]. The effective magnetic field acting on each nanoparticle is then calculated as a superposition of the dipolar contributions  $\vec{B}_{\text{dd}}$  of all other magnetic moments, the static external field  $\vec{B}_{\text{ext}}$ , and the excitation field of the microwave  $\vec{B}_{\text{mw}}(t, f_{\text{ext}})$ . The corresponding theoretical  $\mu$ BLS spectra are obtained by performing a Fourier transformation of the time-dependent magnetization of each particle  $\vec{m}_i(\vec{r}, t)$  over 10 periods for each excitation frequency  $f_{\text{ext}}$  and external static field strength  $B_{\text{ext}}$  followed by the integration of the corresponding amplitude  $A_{\text{FT}}$  over the whole structure.

## III. RESULTS

### A. Circularly shaped MNP arrangement

Figure 2(a) shows a typical frequency dependent  $\mu$ BLS spectrum obtained from the circularly structured arrangement of MNPs shown in Fig. 1(b). The external static magnetic field strength was set to  $B_{\text{ext}} = 230$  mT in the sample plane. The frequency of the externally applied microwave field  $f_{\text{ext}}$  is shown on the horizontal axis, and the frequency shift of the scattered light  $\Delta f_{\text{phot}}$  is shown on the vertical axis. A signal showing an excitation frequency dependence in the range between  $f_{\text{ext}} = 4$  GHz and 12 GHz ( $\Delta f_{\text{phot}} = -4$  GHz and  $-12$  GHz, respectively, Stokes-Signal) is clearly visible, which arises due to resonant excitations within the magnetic system. Integrating the intensities of all  $\Delta f_{\text{phot}}$  for each  $f_{\text{ext}}$ , i.e., summing up each of the vertical lines of the color plot, leads to an integrated  $\mu$ BLS spectrum shown in Fig. 2(b) as the black dashed curve. The other spectrum (blue dashed curve) is obtained by a magnetic field sweep at constant  $f_{\text{ext}}$  and will be discussed in more detail below. Note that the two



spectra shown in Fig. 2(b) belong to two different abscissas as indicated in the figure. In the following only integrated spectra of these two types will be considered, since they contain all the relevant information.

First, we consider the  $f_{\text{ext}}$ -dependent measurement in Fig. 2(b). It is clearly visible that in addition to the main signal a satellite resonance with lower intensity can be identified. Fitting the integrated  $\mu\text{BLS}$  spectrum with two Lorentzian curves (black continuous curve), the resonance frequency of the main peak located at  $f_{\text{ext},M}^{\text{res}} = 9.1$  GHz and of the satellite peak located at  $f_{\text{ext},S}^{\text{res}} = 6.6$  GHz can be extracted. The resonance condition for each MNP is given by

$$\begin{aligned} \frac{\omega_{\text{ext}}^{\text{res}}}{\gamma} &= B_{\text{eff}}^{\text{res}} \\ &= B_{\text{ext}}^{\text{const}} + B_{\text{int}} \\ &= B_{\text{ext}}^{\text{const}} + B_{\text{dd}}, \end{aligned} \quad (1)$$

where  $B_{\text{eff}}^{\text{res}}$  denotes the effective local magnetic field at resonance,  $\omega_{\text{ext}}^{\text{res}} (=2\pi f_{\text{ext}}^{\text{res}})$  the angular excitation frequency of the microwave field,  $\gamma = ge/2m$  the gyromagnetic ratio,  $g$  the Landé factor,  $e$  the elementary charge, and  $m$  the mass of the electron. The effective local magnetic field at resonance is given as the sum of the constant external magnetic field  $B_{\text{ext}}^{\text{const}}$  and the internal magnetic field  $B_{\text{int}}$ . Since the MNPs are not exchange coupled,  $B_{\text{int}}$  arises only due to the dipolar interaction between neighboring MNPs and therefore,  $B_{\text{int}} = B_{\text{dd}}$ . As the two signals occur at different resonance frequencies  $f_{\text{ext},S/M}^{\text{res}}$  at constant  $B_{\text{ext}}^{\text{const}}$ , the two resonances can be attributed to different internal dipole fields  $B_{\text{dd}}$  and thus to MNPs residing in different local environments within the arrangement. It can be concluded that the satellite peak arises from locations with lower dipole fields which lead to a lower resonance frequency than that of the main peak. This is a strong indication that the satellite peak originates from the edges of the MNP arrangement, while the main signal can be interpreted as a resonant excitation of the bulk of the MNP system [36], which will be discussed in more detail below.

In addition to the  $f_{\text{ext}}$ -dependent measurement, the blue curves in Fig. 2(b) show an external field dependent spectrum (blue dashed curve) recorded at a constant excitation frequency  $f_{\text{ext}}^{\text{const}} = 9$  GHz. As  $f_{\text{ext}}^{\text{const}}$  is kept constant and a sweep of the external static field  $B_{\text{ext}}$  is performed, the spectral features change. This can be explained by rearranging the resonance condition in Eq. (1)

$$\begin{aligned} B_{\text{ext}}^{\text{res}} + B_{\text{dd}} &= \frac{\omega_{\text{ext}}^{\text{const}}}{\gamma} \\ B_{\text{ext}}^{\text{res}} &= \frac{\omega_{\text{ext}}^{\text{const}}}{\gamma} - B_{\text{dd}}, \end{aligned} \quad (2)$$

where  $B_{\text{ext}}^{\text{res}}$  denotes the external magnetic field strength at which the resonance occurs. As  $\omega_{\text{ext}}^{\text{const}}/\gamma$  is kept constant, areas which experience lower dipole fields such as the edges will be in resonance at higher external fields  $B_{\text{ext}}^{\text{res}}$  than those with larger dipole fields such as the center of the structure. Therefore, the main peak, which is attributed to the central region of the structure, will appear at lower external field strengths in the spectrum compared to the satellite peak. Fitting the data with two Lorentzian curves (blue continuous

lines), the resonance fields of the main peak of  $B_{\text{ext},M}^{\text{res}} = 230$  mT and of the satellite peak of  $B_{\text{ext},S}^{\text{res}} = 320$  mT can be extracted. Using Eq. (2) for the  $B_{\text{ext}}$ -dependent measurement, the dipole fields of the two resonances can be calculated. Inserting the corresponding values for  $B_{\text{dd}}$  into Eq. (1) for the  $f_{\text{ext}}$ -dependent measurement, the resonance frequencies of the main and the satellite peak are expected to be  $f_{\text{ext},M/S}^{\text{res}} = 9$  GHz and 6.5 GHz, respectively. Although the shape of the spectrum is slightly changed, these values are in good agreement with the results of the frequency dependent measurements.

In order to confirm the interpretation of the experimental findings, micromagnetic simulations were carried out for a model system to analyze the  $f_{\text{ext}}$  and  $B_{\text{ext}}$ -dependent properties of the circularly structured MNP arrangement shown in Fig. 1. The model system comprises one layer of MNPs, forming a circle with a diameter of 300 nm. Within the circle the MNPs are hexagonally arranged, i.e., densely packed. Figure 2(c) shows the simulated  $f_{\text{ext}}$  (black curve) and  $B_{\text{ext}}$ -dependent spectra (blue curve) of the circularly shaped model arrangement. The  $f_{\text{ext}}$ -dependent spectrum is calculated for an external field strength of  $B_{\text{ext}} = 200$  mT. Similar to the  $\mu\text{BLS}$  measurement shown in Fig. 2(b), the calculated  $\mu\text{BLS}$  spectrum also exhibits two peaks. The main peak is located at a resonance frequency of  $f_{\text{ext},M}^{\text{res}} = 9.75$  GHz and the satellite peak at  $f_{\text{ext},S}^{\text{res}} = 7.5$  GHz. Furthermore, the intensity of the satellite peak is lower with respect to the main peak, which reflects the characteristics deduced from the  $\mu\text{BLS}$  experiments. Sweeping  $B_{\text{ext}}$  instead of  $f_{\text{ext}}$  and keeping the excitation frequency constant at 9.75 GHz, an external field dependent spectrum is calculated. As in the case of the  $B_{\text{ext}}$ -dependent experiment shown in Fig. 2(b), a slightly changed shape of the modeled spectrum can be noticed, but the resonance positions of the main and the satellite peak at  $B_{\text{ext},M}^{\text{res}} = 200$  mT and  $B_{\text{ext},S}^{\text{res}} = 280$  mT are again in good agreement with the resonance condition.

The assignment of the main and the satellite signal to the central region and the edge of a single circularly shaped MNP assembly can be confirmed by exploiting a major strength of  $\mu\text{BLS}$  microscopy, i.e., obtaining two-dimensional mappings of the scattered light at a given constant frequency  $f_{\text{ext}}$  and field strength  $B_{\text{ext}}$ . Such mappings have been performed at the resonance frequencies of the main and satellite signals for a circularly shaped MNP assembly with a diameter of 450 nm. The two maps are shown in the top images of Fig. 3. Note that each pixel of the 2D maps is a convolution of the laser spot with the local activity at  $f_{\text{ext}}$  at different positions within the MNP assembly. Therefore, the spatial resolution is limited to that of the laser spot prior to a deconvolution of the spatial intensity maps. Nevertheless, a broader distribution of high intensities is expected for the satellite peak in case it originates from the edge, while a more centered intensity distribution is expected for the main resonance if it originates from the center of the MNP structure. In the 2D maps each pixel has a lateral length of 20 nm. The lower two graphs of Fig. 3 depict the intensities measured along the highlighted red [1] and purple [2] lines for the satellite (black curve) and the main resonance (blue curve). It can be seen that the intensity distribution of the satellite resonance shows a broader distribution than the main resonance underlining that the satellite resonance originates from the edges of the MNP system, while the main

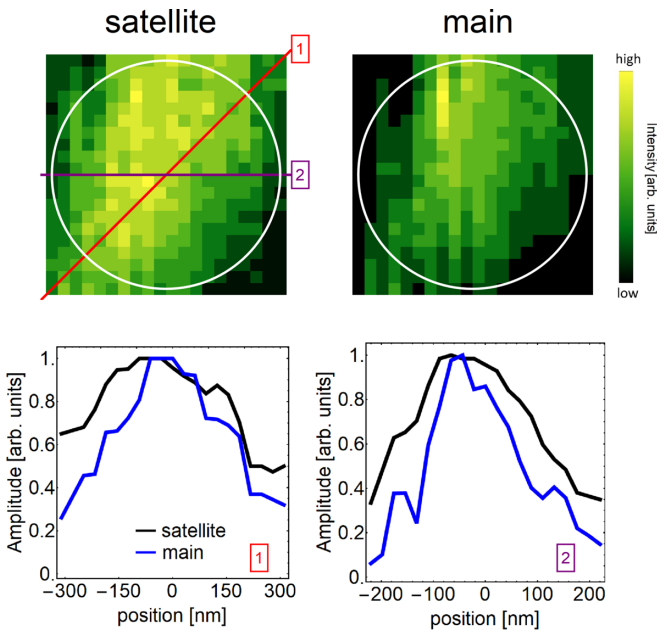


FIG. 3. Top: Spatial maps of the scattered light intensity at the frequency of the satellite peak (left) and the main peak (right) obtained at constant  $B_{\text{ext}}$  of a circular MNP assembly with a diameter of 450 nm. The white circle indicates the boundary of the MNP assembly and each pixel is 20 nm wide. Bottom: Line scans of the scattered light intensity at the two resonances along the red line [1] and the purple line [2] shown in the top image.

resonances corresponds to an oscillation of the bulk (see also Fig. S1 in the Supplemental Material and the corresponding discussion [44]).

### B. Nonstructured, layered MNP arrangement

To corroborate the influence of the edges on the spectral features, we will now compare the observed characteristics

of a structured MNP arrangement with those of a nonstructured one. A corresponding scanning electron microscope image of the layered structure is included in the Supplemental Material in Fig. S2 [44]. In Fig. 4(a), four  $f_{\text{ext}}$ -dependent spectra recorded at four different external field strengths of the nonstructured MNP arrangement are shown as dashed curves. The spectrum taken at  $B_{\text{ext}} = 110$  mT (black curve) is considered first. The two resonances are again clearly visible in this spectrum and the corresponding resonance frequencies are obtained by fitting the experimental spectra by two Lorentzian lines, resulting in  $f_{\text{ext,S/M}}^{\text{res}} = 3.6$  GHz and 6.2 GHz. When increasing  $B_{\text{ext}}$  from 110 mT to 170 mT (red curve), the characteristics of the spectral features changes. First, the resonance positions shift to higher  $f_{\text{ext}}$ , as a result of the altered resonance condition in Eq. (1). Second, at the higher  $B_{\text{ext}}$  of 170 mT, the ratio of the intensities of the satellite peak with respect to the main peak  $A_S/A_M$  is decreased compared to  $B_{\text{ext}} = 110$  mT. Furthermore, the linewidth of the satellite peak  $\sigma_S$  increases from  $\sigma_S = 0.3$  GHz to 0.8 GHz, while the linewidth of the main peak  $\sigma_M$  decreases from  $\sigma_M = 1.1$  GHz to 0.9 GHz. A further increase of  $B_{\text{ext}}$  to 230 mT and 300 mT shows that the trends for  $f_{\text{ext,S/M}}^{\text{res}}$ ,  $\sigma_{S/M}$ , and  $A_S/A_M$  continue almost linearly up to 300 mT. The results are summarized in Fig. 4(c).

Comparing the spectrum of the circularly shaped MNP arrangement shown in Fig. 2(b) (black curve) and the spectrum of the nonstructured, layered system at an external field strength of  $B_{\text{ext}} = 230$  mT shown in Fig. 4(a) (blue curve), two differences can be observed. First, the resonance frequencies of the two samples are not the same and differ considerably although the same type of MNPs forming the arrangements are used in the experiment. The resonance frequencies of the circularly shaped assembly are  $f_{\text{ext,S/M}}^{\text{res}} = 6.6$  GHz and 9.1 GHz, whereas those of the nonstructured, layered system are higher,  $f_{\text{ext,S/M}}^{\text{res}} = 7.2$  GHz and 9.7 GHz. This shift is attributed to the different sizes of the two arrangements. Smaller structures experience smaller dipole fields and

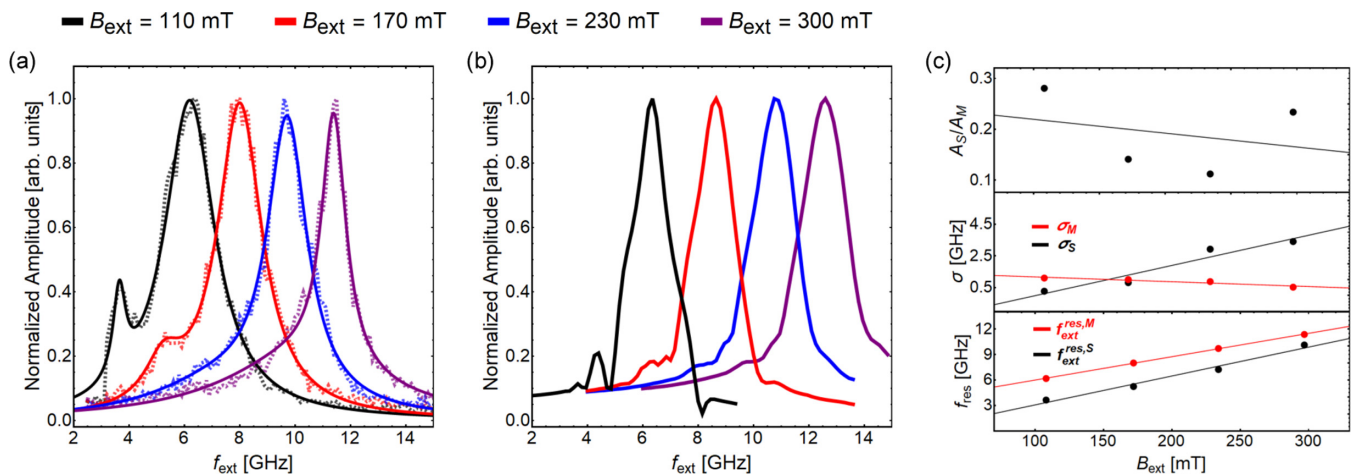


FIG. 4. (a) Integrated  $\mu$ BLS spectra recorded at a nonstructured, layered MNP arrangement at different external field strengths  $B_{\text{ext}}$ . As  $f_{\text{ext}}$  increases, the resonance positions are shifted according to the resonance condition [see Eq. (1)]. The linewidths  $\sigma_{S/M}$  of the two resonances and the ratio of their intensities  $A_S/A_M$  show distinct field dependencies, which are shown in (c). (b) Simulated frequency dependence of nonstructured, layered MNP assemblies at different  $B_{\text{ext}}$ . While at low  $B_{\text{ext}}$  of 100 mT a satellite peak can be recognized, at large  $B_{\text{ext}}$  of 300 mT its presence is only noticeable as an asymmetry in the low frequency range of the spectrum.

thus lower resonance frequencies are required to fulfill the resonance condition. Second, the amplitude of the satellite peak  $A_S$  measured at the circularly shaped MNP assembly is much larger compared to  $A_S$  of the nonstructured system. This also results directly from the size of the assemblies. While in the larger nonstructured system only a small fraction of the MNPs are located near the edges, a much larger fraction of MNPs is located close to the edge of the smaller circularly shaped assembly. This finding further indicates that predominantly MNPs close to the edges contribute to the satellite peak resonance.

To further analyze the observed characteristics at different  $B_{\text{ext}}$  of the nonstructured layered MNP superlattice using micromagnetic simulations, a model system of sufficiently large lateral extension has been defined. This second model system consists of hexagonally arranged moments up to eight layers high and a lateral extension of the entire system of  $1 \mu\text{m}$ . To mimic the spectra more realistically, not all magnetic moments were incorporated in the Fourier transformation, since the area exposed to the photon beam during the  $\mu\text{BLS}$  experiments is only about 300 nm in diameter. Thus, only moments within a cylinder of 300 nm in diameter in the center of the system were included in the Fourier analyses. Figure 4(b) shows the simulated  $f_{\text{ext}}$ -dependent spectra which can be compared with the corresponding experimental data of Fig. 4(a). The spectrum simulated at  $B_{\text{ext}} = 110\text{ mT}$  possesses a main peak at  $f_{\text{ext}} = 6.35\text{ GHz}$  accompanied by a satellite peak of lower intensity, located at  $f_{\text{ext}} = 4.4\text{ GHz}$ . Increasing the external field strength in the simulation leads to an increase of the resonance frequencies of both the main and satellite mode of the spectrum, until only an asymmetric signal remains in the low frequency range of the spectrum due to a merging satellite and the main peak is in good agreement with the observed characteristics from the  $\mu\text{BLS}$  experiments. A possible explanation for the observed merging is that, as the external field strength increases, the angle between the external field and magnetic moments decreases, since their orientation is forced to align parallel to  $B_{\text{ext}}$ . This effect is most pronounced near the edges of the structure and, thus, areas of low dipole fields located near the edges of the MNP arrangement will be reduced in their lateral extensions. As a result, the intensity of the corresponding signal will decrease accompanied with an increase of its linewidth as the coupling to the central region becomes stronger. Furthermore, as  $B_{\text{ext}}$  is increased, disorder of the magnetization orientations due to lattice imperfections and particle size deviations becomes less relevant resulting in a narrowing of the linewidth.

A line narrowing of the main peak from  $\sigma_M = 1.1\text{ GHz}$  at  $B_{\text{ext}} = 110\text{ mT}$  to  $\sigma_M = 0.6\text{ GHz}$  at  $B_{\text{ext}} = 300\text{ mT}$  was observed in the experiment [Fig. 4(a)]. Such a line narrowing could not be observed in the simulated spectra of the ideal model system. Instead we even observe a slight increase of the linewidth in the simulated spectra from 0.6 GHz to 0.8 GHz. The line narrowing in the experiment is very likely due to deviations of the real MNP arrangement from the ideal hexagonal arrangement of alike MNPs in terms of their positions, lattice imperfections, and particle sizes. With increasing magnetic field strength, which aligns the magnetizations, the disorder leading to line broadening becomes less significant in relation to the field effects leading to line narrowing. As a

consequence, the strong line narrowing arises in the experiment with increasing external field strength. It is not present in the simulations because of the lack of disorder in the ideal MNP arrangement assumed as the model system. For this reason the linewidth of the simulated spectra hardly changes. That it is slightly larger at 300 mT is presumably due to the smaller system size than in the experiment.

### C. Influence of the external field strength on the different resonances

In order to analyze in more detail which areas of the arrangement contribute to the two different resonances, the circularly shaped model system based on a MNP monolayer with a diameter of 300 nm is considered again. In Fig. 5(a) simulations of two frequency-dependent  $\mu\text{BLS}$  spectra are shown. The spectra were derived for two different external field strengths of  $B_{\text{ext}} = 200\text{ mT}$  (black curve) and  $500\text{ mT}$  (blue curve). The spectrum simulated at  $B_{\text{ext}} = 200\text{ mT}$  is the same as in Fig. 2(c). As observed for the nonstructured layered MNP arrangement, the resonance frequencies shift to higher frequencies as the external field strength is increased. Furthermore, increasing  $B_{\text{ext}}$  results in a decrease of the ratio of the intensity of the satellite peak with respect to that of the main peak  $A_S/A_M$ . Deeper insight into the spectral features is obtained by analyzing the local activity within the magnetic structure at the corresponding resonance frequencies. Performing a two-dimensional Fourier transformation at the resonance fields of both spectra in Fig. 5(a), the excitation patterns of the resonances labeled M and S for ‘main’ and ‘satellite,’ respectively, are obtained for both fields. The four patterns are shown in Fig. 5(b). The excitation pattern of the main resonances (M-200 mT and M-500 mT) clearly shows that the main resonance originates from particles located in the center of the structure, while the satellite resonances (S-200 mT and S-500 mT) originate from MNPs located near the edge of the structure (see also Fig. S1 and the corresponding discussion of the Supplemental Material). The excitation patterns of the main resonance for the two different  $B_{\text{ext}}$  are very similar, except that the areas of highest activity are slightly larger for  $B_{\text{ext}} = 500\text{ mT}$  than for  $B_{\text{ext}} = 200\text{ mT}$ . In contrast, the excitation pattern of the satellite resonance (S-200 mT and S-500 mT) shows a decrease of the active area with increasing  $B_{\text{ext}}$ . This finding also explains the decrease of the ratio of the intensities  $A_S/A_M$ , since less particles near the edge of the structure contribute to the intensity of the satellite resonance with increasing  $B_{\text{ext}}$ . As the external field strength increases, the magnetic moment of each particle is forced to align with  $B_{\text{ext}}$ . As a consequence, the oscillation amplitude of each particle in the direction perpendicular to the sample plane denoted as the  $z$  axis decreases. Analyzing the dipole field caused by the mutual dipole interaction between the individual particles gives further insight into the observed characteristics. The dipole field  $B_{\text{dd}}$  acting on the particles is calculated over one period  $T = 1/f_{\text{ext}}$  of the microwave field for the resonances S-200 mT and S-500 mT with  $f_{\text{ext}} = 7.5\text{ GHz}$  and  $15.6\text{ GHz}$ , respectively. Subsequently, the dipole fields of particles with the same  $r_x$  value (meaning particles of the same column) are averaged and normalized to the amplitude of the microwave field  $B_{\text{mw}} = 2\text{ mT}$ . Figure 5(c)

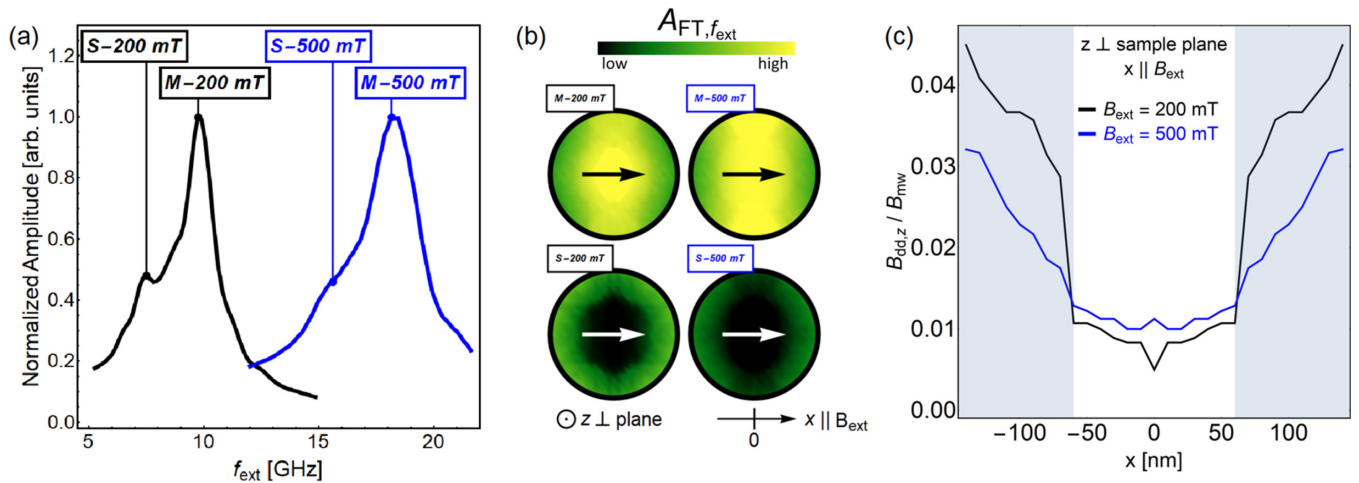


FIG. 5. (a) Simulated  $f_{\text{ext}}$ -dependent  $\mu$ BLS spectra of a circularly shaped monolayer of MNPs with a radius of 150 nm. The spectra were calculated at  $B_{\text{ext}} = 200$  mT (black curve) and 500 mT (blue curve). Increasing  $B_{\text{ext}}$  results in a shift of the resonance position according to the resonance condition [Eq. (1)]. In addition, a decrease of the intensity of the satellite peak with increasing  $B_{\text{ext}}$  is visible. (b) Performing 2D-Fourier analyses unveils the active regions of the two resonances. As  $B_{\text{ext}}$  increases, the active areas of the satellite resonance decrease resulting in a reduction of its relative intensity, compared with the main resonance. The arrows indicate the direction of the external field pointing in the plane of the structure in the  $x$  direction. (c) Averaged dipole field  $\vec{B}_{\text{dd},z}$  in the direction perpendicular to the sample plane ( $z$  axis) over one period  $T = 1/f_{\text{ext}}$  with  $f_{\text{ext}} = 7.5$  GHz and 15.6 GHz (S-200 mT and S-500 mT). The vertical axis is normalized to the strength of the microwave field  $B_{\text{mw}} = 2$  mT.

shows the averaged  $z$  component of the dynamic dipole field  $B_{\text{dd}}$  of each column of the model system as a function of the  $x$  position of the column as indicated in the lower panel of Fig. 5(b). As  $B_{\text{ext}} \parallel x$  increases from 200 mT (black curve) to 500 mT (blue curve), the averaged  $B_{\text{dd}} \parallel z$  near the edges of the structure decreases, whereas only slight variations in the center of the structure are observable. It follows that, as the external field strength increases, the difference of the averaged dipole field diminishes with respect to those of the center. Thus, the capability to respond to the microwave field of MNPs near the edge of the structure decreases, which results in the observed merging of the satellite resonance and the main resonance at high external field strengths.

#### IV. CONCLUSIONS

We investigated the dynamic response of hexagonally ordered, circularly structured MNP arrangements utilizing  $\mu$ BLS microscopy. Depending on the external conditions, two resonances appear in the spectra, which can be attributed to different areas within the magnetic system. While the main resonance originates from the central region of the MNP arrangement, the observed satellite resonance is assigned to magnetic particles near the edges of the system. Frequency dependent measurements were carried out at various external fields, revealing a distinct dependence on the external

magnetic field strength. Micromagnetic simulations unveiled the different characteristics of the dipolar coupling between the MNPs within the different locations of the arrangement. The dipolar coupling between the MNPs has a major impact on the lineshape of the  $\mu$ BLS spectra. Increasing the external field strength leads to a reduction of the effective areas of lower internal magnetic fields accompanied with a reduction of the intensity of the corresponding satellite resonance compared to the main resonance. Thus, it has been demonstrated that the response of the MNP arrangement is very sensitive to an external magnetic field and the frequency of the microwave excitation. A full understanding of these dependencies is essential for successfully incorporating such magnetic structures into devices. In the future, we plan to extend our studies to higher frequency shifts of the scattered light. Such studies may then yield information about excitations of the exchange-coupled atomic magnetic moments within the individual MNPs.

#### ACKNOWLEDGMENTS

We acknowledge computational resources provided by the HPC Core Facility and the HRZ of the Justus-Liebig-University Giessen. In addition, the authors thank Marcel Giar and Philipp Risius (HPC Core Facility, Justus Liebig University Giessen) for their administrative support.

- [1] J.-H. Choi, H. Wang, S. J. Oh, T. Paik, P. S. Jo, J. Sung, X. Ye, T. Zhao, B. T. Diroll, C. B. Murray, and C. R. Kagan, Exploiting the colloidal nanocrystal library to construct electronic devices, *Science* **352**, 205 (2016).
- [2] C. R. Kagan, E. Lifshitz, E. H. Sargent, and T. V. Talapin, Building devices from colloidal quantum dots, *Science* **353**, aac5523 (2016).

- [3] H. Zeng, C. T. Black, R. L. Sandstrom, P. M. Rice, C. B. Murray, and S. Sun, Magnetotransport of magnetite nanoparticle arrays, *Phys. Rev. B* **73**, 020402(R) (2006).
- [4] C. Jiang, S. M. Ng, C. W. Leung, and P. W. T. Pong, Magnetically assembled iron oxide nanoparticle coatings and their integration with pseudo-spin-valve thin films, *J. Mater. Chem. C* **5**, 252 (2017).



- [5] T. Paik, H. Yun, B. Fleury, S.-H. Hong, P. S. Jo, Y. Wu, S.-J. Oh, M. Cargnello, H. Yang, C. B. Murray, and C. R. Kagan, Hierarchical materials design by pattern transfer printing of self-assembled binary nanocrystal superlattices, *Nano Lett.* **17**, 1387 (2017).
- [6] B. H. Zhou and J. D. Rinehart, Pseudo spin valve behavior in colloiddally prepared nanoparticle films, *ACS Appl. Electron. Mater.* **1**, 1065 (2019).
- [7] M. Fischer, M. T. Elm, S. Sakita, S. Hara, and P. J. Klar, Magnetoresistance effects and spin-valve like behavior of an arrangement of two MnAs nanoclusters, *Appl. Phys. Lett.* **106**, 032401 (2015).
- [8] M. T. Elm, S. Hara, Transport properties of hybrids with ferromagnetic MnAs nanoclusters and their potential for new magnetoelectronic devices, *Adv. Mater.* **26**, 8079 (2014).
- [9] K. Yakushiji, F. Ernult, H. Imamura, K. Yamane, S. Mitani, K. Takanashi, S. Takahashi, S. Maekawa, and H. Fujimori, Enhanced spin accumulation and novel magnetotransport in nanoparticles, *Nat. Mater.* **4**, 57 (2005).
- [10] G. Song, M. Ranjbar, D. R. Daughton, and R. A. Kiehl, Nanoparticle-induced anomalous Hall effect in graphene, *Nano Lett.* **19**, 7112 (2019).
- [11] A. Dong, J. Chen, P. M. Vora, J. M. Kikkawa, and C. B. Murray, Binary nanocrystal superlattice membranes self-assembled at the liquid-air interface, *Nature (London)* **466**, 474 (2010).
- [12] L. Giovannini, F. Montoncello, and F. Nizzoli, Effect of interdot coupling on spin-wave modes in nanoparticle arrays, *Phys. Rev. B* **75**, 024416 (2007).
- [13] C. Michel, M. T. Elm, B. Goldlücke, S. D. Baranovskii, P. Thomas, W. Heimbrodt, and P. J. Klar, Tailoring the magnetoresistance of MnAs/GaAs:Mn granular hybrid nanostructures, *Appl. Phys. Lett.* **92**, 223119 (2008).
- [14] M. A. Boles, M. Engel, and D. V. Talapin, Self-assembly of colloidal nanocrystals: From intricate structures to functional materials, *Chem. Rev.* **116**, 11220 (2016).
- [15] A. Dong, J. Chen, S. J. Oh, W. K. Koh, F. Xiu, X. Ye, D. K. Ko, K. L. Wang, C. R. Kagan, and C. B. Murray, Multiscale periodic assembly of striped nanocrystal superlattice films on a liquid surface, *Nano Lett.* **11**, 841 (2011).
- [16] E. Shevchenko, D. V. Talapin, N. A. Kotov, S. O'Brien, and C. B. Murray, Structural diversity in binary nanoparticle superlattices, *Nature (London)* **439**, 55 (2006).
- [17] X. Ye, C. Zhu, P. Ercius, S. N. Raja, B. He, M. R. Jones, M. R. Hauwiller, Y. Liu, T. Xu, and P. A. Alivisatos, Structural diversity in binary superlattices self-assembled from polymer-grafted nanocrystals, *Nat. Commun.* **6**, 10052 (2015).
- [18] S. Mamica, M. Krawczyk, M. L. Sokolovskyy, and J. Romero-Vivas, Large magnonic band gaps and spectra evolution in three-dimensional magnonic crystals based on magnetoferritin nanoparticles, *Phys. Rev. B* **86**, 144402 (2012).
- [19] F. Vernay and H. Kachkachi, Single-particle versus collective effects in assemblies of nanomagnets: Screening, *J. Magn. Magn. Mater.* **500**, 166286 (2020).
- [20] B. W. Zingsem, T. Feggeler, A. Terwey, S. Ghaisari, D. Spoddig, D. Faivre, R. Meckenstock, M. Farle, and M. Winklhofer, Biologically encoded magnonics, *Nat. Commun.* **10**, 4345 (2019).
- [21] S. Tacchi, G. Gubbiotti, M. Madami, and G. Carlotti, Brillouin light scattering studies of 2D magnonic crystals, *J. Phys.: Condens. Matter* **29**, 073001 (2017).
- [22] J. Chen, A. Dong, J. Cai, X. Ye, Y. Kang, J. M. Kikkawa, and C. B. Murray, Collective dipolar interactions in self-assembled magnetic binary nanocrystal superlattice membranes, *Nano Lett.* **10**, 5103 (2010).
- [23] Z. Yang, J. Wei, P. Bonville, and M. P. Pileni, Engineering the magnetic dipolar interactions in 3D binary supracrystals via mesoscale alloying, *Adv. Funct. Mat.* **25**, 4908 (2015).
- [24] M. Anand, J. Carrey, and V. Banerjee, Role of dipolar interactions on morphologies and tunnel magnetoresistance in assemblies of magnetic nanoparticles, *J. Magn. Magn. Mater.* **454**, 23 (2018).
- [25] H. T. Nguyen, and M. G. Cottam, Dipole-exchange spin waves in ferromagnetic nanostructures with spherical geometries, *Surf. Rev. Lett.* **15**, 727 (2008).
- [26] P. Poddar, T. Telem-Shafir, T. Fried, and G. Markovich, Dipolar interactions in two- and three-dimensional magnetic nanoparticle arrays, *Phys. Rev. B* **66**, 060403(R) (2002).
- [27] P. Bender, E. Wetterskog, D. Honecker, J. Fock, C. Frandsen, C. Moerland, L. K. Bogart, O. Posth, W. Szczerba, H. Gavilan, R. Costo, M. T. Fernandez-Diaz, D. González-Alonso, L. Fernandez Barquin, and C. Johansson, Dipolar-coupled moment correlations in clusters of magnetic nanoparticles, *Phys. Rev. B* **98**, 224420 (2018).
- [28] K. L. Krycka, J. J. Rhyne, S. D. Oberdick, A. M. Abdelgawad, J. A. Borchers, Y. Ijiri, S. A. Majetich, and J. W. Lynn, Spin waves across three-dimensional, close-packed nanoparticles, *New J. Phys.* **20**, 123020 (2018).
- [29] G. Singh, H. Chan, A. Baskin, E. Gelman, N. Reppin, P. Kral, and R. Klajn, Self-assembly of magnetite nanocubes into helical superstructures, *Science* **345**, 1149 (2014).
- [30] R. Moreno, S. Poyser, D. Meilak, A. Meo, S. Jenkins, V. K. Lazarov, G. Vallejo-Fernandez, S. Majetich, and R. F. L. Evans, The role of faceting and elongation on the magnetic anisotropy of magnetite Fe<sub>3</sub>O<sub>4</sub> nanocrystals, *Sci. Rep.* **10**, 2722 (2020).
- [31] S. D. Oberdick, A. Abdelgawad, C. Moya, S. Mesbahi-Casey, D. Kepaptsoglou, V. K. Lazarov, R. F. L. Evans, D. Meilak, E. Skoropata, J. van Lierop, I. Hunt-Isaak, H. Pan, Y. Ijiri, K. L. Krycka, J. A. Borchers, and S. A. Majetich, Spin canting across core/shell Fe<sub>3</sub>O<sub>4</sub>/Mn<sub>x</sub>Fe<sub>3-x</sub>O<sub>4</sub> nanoparticles, *Sci. Rep.* **8**, 3425 (2018).
- [32] J. Pang, S. Xiong, F. Jaekel, Z. Sun, D. Dunphy, and C. J. Brinker, Free-standing, patternable nanoparticle/polymer monolayer arrays formed by evaporation induced self-assembly at a fluid interface, *J. Am. Chem. Soc.* **130**, 3284 (2008).
- [33] A. V. Chumak, V. I. Vasyuchka, A. A. Serga, and B. Hillebrand, Magnon spintronics, *Nat. Phys.* **11**, 453 (2015).
- [34] Q. Wang, P. Pirro, R. Verba, A. Slavin, B. Hillebrand, and A. V. Chumak, Reconfigurable nanoscale spin-wave directional coupler, *Science Adv.* **4**, e1701517 (2018).
- [35] T. Sebastian, K. Schultheiss, B. Obry, B. Hillebrands, and H. Schultheiss, Micro-focused Brillouin light scattering: imaging spin waves at the nanoscale, *Frontiers in Physics* **3**, 35 (2015).
- [36] N. Neugebauer, A. Fabian, M. T. Elm, D. M. Hofmann, M. Czerner, C. Heiliger, and P. J. Klar, Investigation of the dipole interaction in and between ordered arrangements of magnetic nanoparticles, *Phys. Rev. B* **101**, 104409 (2020).
- [37] A. Fabian, M. Czerner, C. Heiliger, M. T. Elm, D. M. Hofmann, and P. J. Klar, Domain formation in rectangular-magnetic nanoparticle assemblies, *Phys. Rev. B* **98**, 054401 (2018).



- [38] K. M. Krishnan, A. B. Pakhomov, Y. Bao, P. Blomqvist, Y. Chun, M. Gonzales, K. Griffin, X. Ji, and B. K. Roberts, Nanomagnetism and spin electronics: Materials, microstructure and novel properties, *J. Mater. Sci.* **41**, 793 (2006).
- [39] S. Singamaneni, V. Bliznyuk, C. Binek, and E. Y. Tsybmal, Magnetic nanoparticles : Recent advances in synthesis, self-assembly and applications, *J. Mater. Chem.* **21**, 16819 (2011).
- [40] Z. Nedelkoski, D. Kepaptsoglou, L. Lari, T. Wen, R. A. Booth, S. D. Oberdick, P. L. Galindo, Q. M. Ramasse, R. F. L. Evans, S. Majetich, and V. K. Lazarov, Origin of reduced magnetization and domain formation in small magnetite nanoparticles, *Sci. Rep.* **7**, 45997 (2017).
- [41] S. Sun, H. Zeng, D. B. Robinson, S. Raoux, P. M. Rice, S. X. Wang, and G. Li, Monodisperse  $MFe_2O_4$  (M = Fe, Co, Mn) Nanoparticles, *J. Am. Chem. Soc.* **126**, 273 (2004).
- [42] X. Batlle, N. Perez, P. Guardia, O. Iglesias, A. Labarta, F. Bartolome, L. M. Garcia, J. Bartolome, A. G. Roca, M. P. Morales, and C. J. Serna, Magnetic nanoparticles with bulklike properties, *J. Appl. Phys.* **109**, 07B524 (2011).
- [43] R. F. L. Evans, W. J. Fan, P. Chureemat, T. A. Ostler, and R. W. Chantrell, Atomistic spin model simulations of magnetic nanomaterials, *J. Phys.: Condens. Matter* **26**, 103202 (2014).
- [44] See Supplemental Material at <http://link.aps.org/supplemental/10.1103/PhysRevB.103.094438> for a more detailed analysis of the 2D-BLS maps of the main and the satellite resonance and a discussion of the lattice defects of the nonstructured, layered MNP arrangement.